Materials Today Bio 17 (2022) 100491

Contents lists available at ScienceDirect

Materials Today Bio

journal homepage: www.journals.elsevier.com/materials-today-bio

Janus electro-microenvironment membrane with surface-selective osteogenesis/gingival healing ability for guided bone regeneration

Chunhua Lai [a,1], Mingwei Cheng [a,1], Chengyun Ning [b], Yiheng He [a], Zhengnan Zhou [b], Zhaoyi Yin [c], Peijun Zhu [a], Yan Xu [a], Peng Yu [b,**], Shulan Xu [a,*]

[a] Center of Oral Implantology, Stomatological Hospital Southern Medical University, Guangzhou, 510280, China
[b] School of Material Science and Engineering, South China University of Technology, Guangzhou, 510641, China
[c] School of Materials Science and Engineering, Kunming University of Science and Technology, Kunming, 650093, China

ARTICLE INFO

Keywords:
Electric microenvironment
Piezoelectric
Guided bone regeneration
Osteogenic
Janus membrane

ABSTRACT

Guided bone regeneration is widely applied in clinical practice to treat alveolar bone defects. However, the rate of healing of severe alveolar bone defects is slow, and there is a high incidence of soft tissue wound dehiscence. In this study, we propose a barrier membrane with a Janus electro-microenvironment (JEM) to achieve side-selective bone regeneration and soft tissue healing. The JEM membrane was constructed using a polarized polyvinylidene fluoride ferroelectric membrane with different surface potentials on either side. It promoted osteogenic differentiation and bone regeneration on the negatively polarized side (JEM-) and soft tissue regeneration on the positively polarized side (JEM+). Further investigation revealed that the JEM-mediated promotion of bone formation was related to mitochondrial autophagy, as indicated by depolarization of the mitochondrial membrane potential and the expression of LC3, Pink I, and Parkin. Moreover, the gingival healing promoted by JEM+ was related to oxidative phosphorylation in mitochondria, as indicated by the upregulation of mitochondrial complexes I–V and an increase in ATP generation. The design concept of the JEM provides a new avenue for regulating tissue regeneration between different tissue interfaces.

1. Introduction

Alveolar bone defect repair constitutes a great challenge in the field of dental implants. To reconstruct a microenvironment for bone regeneration during alveolar bone defects, guided bone regeneration (GBR) is widely used in clinical practice. In this method, a barrier membrane is placed between the bone defect and gingival tissue with minimal damage and a low probability of complications. Despite advances in the treatment of defects through GBR, severe alveolar bone defects continue to exhibit a slow healing process. To address this problem, researchers have attempted to modify barrier membranes with the addition of growth factors or chemicals to promote healing. However, these modifications are reported to cause extensive soft tissue hematomas, toxic reactions, and secondary damage to normal tissue in the affected area [1–3].

Severe bone defects are usually accompanied by soft tissue atrophy. During GBR, the tension in the soft tissue increases when the barrier membrane above the bone graft is covered with soft tissue, which is likely to cause postoperative complications. The incidence of GBR-associated wound dehiscence and bio-membrane exposure is reportedly 22.7% [4–6], leading to bacterial colonization and compromising bone regeneration, eventually causing bone augmentation failure [7]. Therefore, improving gingival healing and stimulating bone regeneration are two-fold challenges in treating severe alveolar bone defects. The key to addressing this problem lies in reconstructing the microenvironment using a barrier membrane with a two-sided design for achieving bone regeneration and gingival healing, respectively, for GBR.

Both osteoblasts and fibroblasts, involved in the growth of bone and soft tissue, respectively, respond to electric stimuli, and bioelectric signals could be critical for mediating their growth [8]. Several studies have shown that the application of external current and electrical stimuli can induce bone formation and promote fracture healing [9–11]. In orthopedics, electrical stimulation has been used to treat bone nonunion [12–14]. In addition, electrical signals regulate the proliferation and migration of fibroblasts and stimulate them to secrete collagen, which

* Corresponding author.
** Corresponding author.
E-mail addresses: imyup@scut.edu.cn (P. Yu), 672588@smu.edu.cn (S. Xu).
[1] These authors contributed equally to this work.

https://doi.org/10.1016/j.mtbio.2022.100491
Received 12 August 2022; Received in revised form 6 November 2022; Accepted 9 November 2022
Available online 13 November 2022

promotes wound healing [15,16]. These studies indicate the possibility of designing innovative barrier membranes with different electrical properties. Furthermore, recent studies have focused on utilizing the intrinsic electric properties of biomaterials to regulate cell activity and tissue regeneration [17–20]. Thus, we hypothesized that selective bone regeneration and soft tissue healing can be effectively achieved by designing strategies involving the manipulation of electric properties on barrier membranes to generate an electric microenvironment.

The current generation of GBR membranes are designed to exhibit space-maintaining properties, antibacterial properties, and wound healing and bone regeneration properties [21–23], but lack the ability to induce a Janus electro-microenvironment (JEM) for bone and soft tissue regeneration. Recently, JEM membrane is a hot research topic in GBR application, many studies prepared excellent Janus membranes for GBR, which possessed osteoinduction and barrier functions [23,24]. While improving gingival healing is also important, the rapid healing of gingival ensures new bone formation. Thus, the engineering of JEM GBR membranes (combining built-in localized electrical stimuli with double-side hetero electricity) that can simultaneously induce osteogenesis and enhance gingival healing, eventually achieving a favorable clinical effect, is needed.

Ferroelectric polyvinylidene fluoride (PVDF)-based materials are biocompatible, flexible, and can easily be processed or produced. Their surface potential can also be regulated to enhance bone tissue regeneration [25–28]. As PVDF-based ferroelectric materials exhibit spontaneous polarization characteristics, the direction of an electric dipole can be changed to regulate the surface potential on either side of the membrane. In this study, we propose a JEM-inducing PVDF-based polarized barrier membrane for GBR application. As shown in Scheme 1, after polarization, the JEM P(VDF-TrFE) membrane was inserted between the damaged gingival tissue and the bone defect. Based on the growth properties of osteoblasts and fibroblasts on charged surfaces shown in previous studies, we hypothesized that the JEM membrane can simultaneously promote gingival tissue healing and bone regeneration in alveolar bone defects. The effectiveness of osteogenesis and soft tissue regeneration on the developed JEM membrane and the underlying mechanisms involved were studied *in vitro* and *in vivo*.

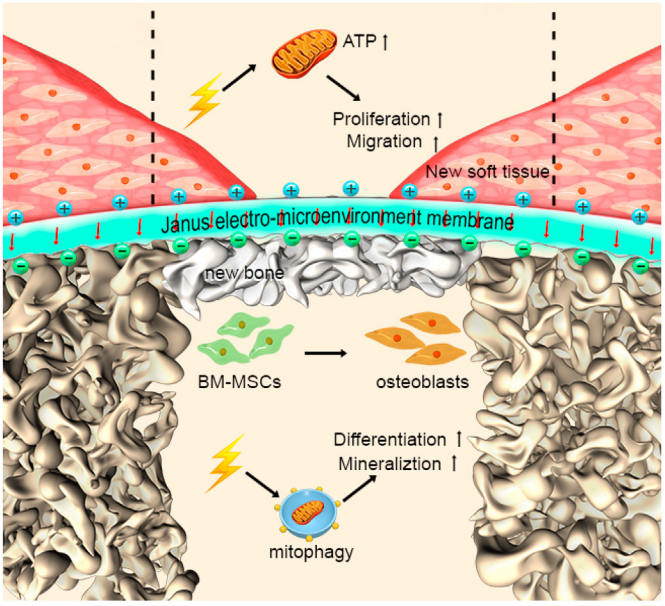

Scheme 1. Schematic illustration of the Janus electro-microenvironment (JEM) membrane. JEM is based on a polarized poly(vinylidene fluoride-co-trifluoroethylene) (P(VDF-TrFE)) membrane to promote surface-selective osteogenesis/gingival healing. The direction of electrical dipoles of the P(VDF-TrFE) membrane is reoriented after external electric field polarization, resulting in the formation of a JEM membrane due to surface potential transition on the different surfaces of the ferroelectric P(VDF-TrFE) membrane. The electro-microenvironment of the positively polarized side of the P(VDF-TrFE) membrane is denoted as JEM(+) and the electro-microenvironment of the negatively polarized side is denoted as JEM(−). When the JEM membrane is placed between the bone defect and gingival tissue defect, JEM(+) promotes soft tissue regeneration by stimulating mitochondrial oxidative phosphorylation, which could produce ATP and provide energy for cellular metabolism and biosynthesis, while JEM(−) promotes bone tissue regeneration by stimulating mitophagy, which could speed up mineral transportation and deposition. The short red arrows denote the direction of an electric dipole in the JEM membrane. Dotted lines denote the boundaries of the new soft tissue formed.

2. Materials and methods

2.1. Fabrication of JEM membranes

poly(vinylidene fluoride-co-trifluoroethylene) (P(VDF-TrFE)) membranes with a thickness of approximately 45–60 μm were fabricated using a solution casting technique, as described previously [29]. P(VDF-TrFE) (70/30 mol%) powder was supplied by Arkema, France. P(VDF-TrFE) powder (2 g) was added to 20 mL of N, N-dimethylformamide. After stirring and heating to 60 °C for 1 h, the suspension was poured on a smooth glass to form a membrane with a consistent thickness. For polarization, a voltage of 6 kV/mm was applied between the electrodes for 1 h, then cooled to 25 °C. By precisely controlling polarization conditions, the epitaxial surfaces of electrical signal response P(VDF-TrFE) membranes with opposite polarization [JEM(+), JEM(−)] were successfully fabricated, and the non-polarized P(VDF-TrFE) membranes were used as the control.

2.2. Characterization of JEM membranes

The JEM membrane was sprayed with a gold layer to improve conductivity, and the surface morphology was observed using a scanning electron microscope (JSM6300, JEOL, Peabody, MA, USA). The phase composition of the JEM membrane was examined using X-ray diffraction (XRD Bruker AXS Inc, Germany). The surface hydrophilicity of the samples was evaluated by water contact angle measurements (Filderstadt OCA15 device), using distilled water as the test liquid. The mechanical properties were assessed using a universal mechanical machine (INSTRON-5967, USA) for tensile and elastic tests. In order to characterize the piezoelectric properties of the P(VDF-TrFE) membrane, the polarization–electric field (P–E) hysteresis loops at room temperature were detected using a ferroelectric tester (TF Analyzer 3000, aixACCT, Germany) under a triangular waveform at a frequency of 0.5 Hz and maximum field amplitude of 8 kV/mm. The piezoelectric coefficient (d_{33}) of JEM membranes was measured by the d_{33} Piezoelectric Measuring Instrument (ZJ-3AN, IACAS, Beijing, China). Scanning Kelvin probe force microscopy (SKPFM) (MFP-3D-SA, Asylum Research, US) was used to quantitative detect the surface potential of P(VDF-TrFE). Pt-coated Si probes (SCM-PIT, spring constant of 4 N m1, Bruker) were used for KPFM measurement.

2.3. Cell culture on JEM membrane

The rat bone marrow-derived mesenchymal stem cells (rBMSCs) (Cyagen Bioscience Inc., Guangzhou, China) were cultured in DMEM supplemented with 10% fetal bovine serum (FBS), 100 mg/mL streptomycin, and 100 units/mL penicillin. The human gingival fibroblasts (hGFs) (ATCC® CRL-2014™ *Homo sapiens* gingival biopsy normal, Manassas, VA, USA) were cultured in DMEM supplemented with 10% FBS, 4.5 g/L glucose, 100 mg/mL streptomycin, and 100 units/mL penicillin. Cells from passages 2–4 were used in the experiments. The culture medium was changed every three days. In all experiments, the JEM membrane was cut into a standard size of 1.5 × 1.5 cm and sterilized with 75% alcohol solution for 4 h.

2.4. Cell proliferation assay

rBMSCs and hGFs were seeded on sterilized JEM membrane at a density of 2×10^4 cells/well in 24-well plates, and cultured for 1, 3, and 5 d. To evaluate cell proliferation, the medium was replaced with a culture medium containing 10% CCK-8 kit solution (Beyotime Biotechnology Inc., Shanghai, China), and incubated at 37 °C for 30 min. The absorbance of each well was recorded at 450 nm using a microplate reader.

2.5. Alkaline phosphatase (ALP) activity assay

rBMSCs were seeded on the sterilized JEM membrane at a density of 5×10^5 cells/well in 12-well plates, and the medium was then replaced with osteogenic differentiation medium, which consisted of complete growth medium, supplemented with 10 mmol/L glycerophosphate, 50 mg/L ascorbic acids, and 100 nmol/L dexamethasones. After culturing for 3 and 7 d, rBMSCs were washed three times with phosphate-buffered saline (PBS). For ALP staining, cells were fixed in 4% paraformaldehyde for 30 min and subsequently stained with ALP staining solution (Beyotime Biotechnology Inc.) for 30 min. ALP activity was evaluated using the ALP assay kit (Beyotime Biotechnology Inc.) according to the manufacturer's instructions. The results are shown as relative ALP activity after normalization with the total protein concentration.

2.6. Alizarin red staining for mineralization

rBMSCs were seeded on the sterilized JEM membrane at a density of 5×10^5 cells/well in 12-wells plates, and the medium was then replaced with an osteogenic differentiation medium. After culturing for 7, 14, and 21 d, cells were fixed in 4% paraformaldehyde for 30 min, and subsequently stained with the Alizarin Red S solution (Sigma-Aldrich, St. Louis, MO, USA) for 30 min. For quantitative analysis, the Alizarin Red stain on the membrane was dissolved in 10% cetylpyridinium chloride (Sigma-Aldrich) and the absorbance was read at a wavelength of 620 nm.

2.7. Cytoskeleton and nucleus staining

rBMSCs and hGFs were seeded on the sterilized JEM membrane at a density of 5×10^5 cells/well in 12-well plates. After culturing for 3 d, cells were washed three times with PBS and subsequently fixed with 4% paraformaldehyde. To image the cytoskeleton, cells were incubated with FITC-Phalloidin (Yeasen, Shanghai, China) for 1 h and subsequently stained with DAPI (Beyotime Biotechnology Inc.) for 10 min, according to the manufacturer's instructions. The images were acquired using a confocal laser scanning microscope (Carl Zeiss, Jena, Germany).

2.8. Quantitative real-time polymerase chain reaction (qPCR) analysis

rBMSCs and hGFs were seeded on the sterilized JEM membrane at a density of 5×10^5 cells/well in 12-well plates, and the medium was then replaced with an osteogenic differentiation medium. Total RNA was isolated using TRIzol reagent (Invitrogen, Waltham, MA, USA) on the indicated days. The RNA was subsequently reverse-transcribed into complementary DNA (cDNA) using a PrimeScript RT reagent kit (Takara Bio Inc., Shiga, Japan). qPCR was performed using a 7500 real-time PCR System (Applied Biosystems, Carlsbad, CA, USA). The mRNA transcripts included in the study were *Runx2*, *Ocn*, *Opn*, *Col 1, Pink1, Parkin, Lc3, FAK, Fn, and Gapdh*. The primer sequences for the same are shown in Table 1. Results were calculated using the 2-ΔΔCt method and presented as fold-change relative to the control (*GAPDH*).

Table 1
Real-time PCR Primer sequences.

Target genes	Forward sequence (5′–3′)	Reverse sequence (5′–3′)
Runx2	GACGAGGCAAGAGTTTCACC	GGTTCCCGAGGTCCATCTAC
Ocn	CTCACACTCCTCGCCCTATT	CGCCTGGGTCTCTTCACTAC
Opn	GCCGAGGTGATAGTGTGGTT	ACTCCTCGCTTTCCATGTGT
Col I	AGAGGAAGGAAAGCGAGGAG	GGACCAGCAACACCATCTG
Pink1	GGACGCTGTTCCTCGTTA	ATCTGCGATCACCAGCCA
Parkin	AACCGGTACCAGCAGTATGG	TTCGCAGGTGACTTTCCTCT
Lc3	AGCAGCATCCAACCAAAA	CTGTGTCCGTTCACCAACAG
FAK	GAAGCCTTGCCAGCCTCA	GTGGGGCTGGCTGGATTT
Fn	GTCAGCCCAACTCCCACC	TTGGTGGCCGTACTGCTG
GAPDH	CTGGAGAAACCTGCCAAGTATG	GGTGGAAGAATGGGAGTTGCT

2.9. Western blotting analysis

Total protein was derived from the rBMSCs and hGFs on the JEM membrane using RIPA buffer (Beyotime Biotechnology Inc.) on the indicated days, and the total protein concentration was evaluated using a BCA protein assay kit (Bestbio, China). Proteins were separated using electrophoresis on a polyacrylamide gel plate and subsequently transferred to polyvinylidene difluoride membranes. The membranes were blocked with 5% BSA and incubated with anti-*RUNX2,* anti-*OPN,* anti-*OCN,* anti-*COL I,* anti-*LC3,* anti-*PINK1*, anti-*Parkin,* anti-*Fak,* anti-*Fn1,* anti-*Complex I, Complex II, Complex III, Complex IV, Complex V* (Abcam, Inc., Cambridge, UK) overnight at 4 °C. The membranes were then washed with TBST solution thrice, and incubated with horseradish peroxidase-conjugated secondary antibodies before visualization. Protein expression levels were normalized to that of GAPDH. The protein bands were visualized using enhanced chemiluminescence (ECL) reagent (Beyotime Biotechnology Inc.). Protein levels were quantified using Image J analysis software.

2.10. Mitochondrial membrane potential assay

rBMSCs were seeded on the sterilized JEM membrane at a density of 2×10^4 cells/well in 12-well plates, and the medium was then replaced with an osteogenic differentiation medium. After culturing for 7 d, the cells were washed with PBS, and the mitochondrial membrane potential (MMP) assay was performed using JC-1 dye (Beyotime Biotechnology Inc.). Briefly, the JC-1 dye solution was mixed according to the manufacturer's instructions, and incubated with the cells at 37 °C for 30 min. For quantitative analysis, cells were collected by trypsin without EDTA and then incubated with the working solution in suspension for 20 min, subsequently resuspended in the basic medium. Fluorescence intensity was measured by flow cytometry and the emission ratio was detected at a ratio of 525/590 nm at six replicated times.

2.11. Transwell assay of hGFs

hGFs were pipetted (2×10^4 cells/well) into the top of the transwell chambers (BD FalconTM Cell Culture Inserts, BD Biosciences, Bedford, MA, USA) for migration analysis. The JEM membrane was placed at the bottom of the chamber which contained 200 μL serum-free medium as a physical attractant. Cells were incubated at 37 °C for 24 h. Cells in the lower membrane were fixed with 4% paraformaldehyde and stained with crystal violet for 30 min. After that, Cells were recorded under a microscope and quantitatively analyzed using ImageJ software.

2.12. Wound healing assay of hGFs

hGFs were seeded on the JEM membrane into a 6-well plate (3×10^4 cells/well) and cultured at 90% cell confluence. A 200 μL sterile pipette tip was used to create an artificial scratch. The scratched areas were observed at 0, 6, 12 and 24 h, respectively. The distance of cell migration was observed under a microscope, and quantitatively analyzed using ImageJ software.

2.13. The mitochondrial function of hGFs

The XF 24 Extracellular Flux Analyzer (Seahorse Bioscience, North Billerica, MA, USA) was used to measure the oxygen consumption rate (OCR). The hGFs were seeded on the membranes at a density of 3×10^4 cells/well in a 6-well plate. After culturing for 1 d, cells were collected using trypsin, seeded (1.2×10^4/well) on XF 24-well microplates, and incubated for 24 h at 37 °C in 5% CO_2. After replacing the medium with bicarbonate-free DMEM XF assay medium, which was supplemented with 10 mM glucose, 2 mM L-glutamine, and 1 mM pyruvate, the plates were pre-warmed at 37 °C. Microplates were pre-incubated in a 37 °C incubator without CO_2 for 1 h prior to the experiment. A total of 56 μL oligomycin was added through port A of the analyzer to each well, along with 62 μL FCCP through port B, and 69 μL rotenone through port C. Each step had three cycles, including mixing for 3 min, waiting for 2 min, and measurement time for 3 min.

2.14. Rat mandibular defect and palatal wound healing experiment

78 six-week-old male SD rats weighing 180 ± 20 g were used for the study. All rats were housed under specific pathogen-free (SPF) conditions at the animal experimental center of Southern Medical University. The research protocol was approved by the Institutional Animal Care and Use Committee of Southern Medical University (Protocol no. 2019080).

For the rat mandibular defect experiment, a total of 24 rats were randomly divided into three groups (n = 8 for each group). To establish mandibular defects, the mandibular angle was exposed and a critical-size bone defect (4 mm) was made by trephine drill under general anesthesia. The mandibular defect was covered with the JEM and the control membrane. The membrane is inserted between the bone and periosteum to cover the defect completely. The muscle and skin were sutured hierarchically to achieve primary healing. All rats were sacrificed at 4 weeks and 8 weeks.

For the rat palatal wound healing experiment, a total of 54 rats were randomly divided into three groups (n = 6 for each group). To establish palatal wound healing defects, a critical round wound (3 mm) was made by biopsy punch under general anesthesia. The mucoperiosteal at the center of the hard palate defects was removed. Finally, the membrane was inserted and fixed under the surrounding mucoperiosteal. During the experiment, we don't observe any changes in the behavior or weight of the rats. All rats were sacrificed at 7, 14, and 21 days.

For micro-computed tomography (micro-CT) scanning, a quantitative micro-CT DELPet μCT 100 scanners (Delta, Taiwan) was used at 80 keV, 114 μA, and an isotropic resolution of 22.5 μm. After three-dimensional reconstruction, the representative sections were cut from a vertical view. Standard resolution mode was used to quantify the microstructural properties of the bone. The results were analyzed using the built-in software. Image J software was used to measure the percentage area of the newly formed bone in each of the measured regions.

A digital camera was used to observe the wound-healing defects and analyze the wound-healing areas at a standard distance and magnification. A scientific ruler was also placed within the photographic area to confirm accuracy. The wound margins (unhealed area) were marked to calculate the mean wound surface area with Image J using the ruler in the photograph as a scale reference.

All samples were fixed in 4% paraformaldehyde for 1 d. Samples of mandibular and palatal defects were dissected and decalcified in 10% EDTA for 8 w, and then 18% EDTA for 2 w. After dehydration through a graded ethanol series, the tissues were embedded in paraffin. All specimens were continuously sectioned along the axial plane at 4 μm intervals, until the defect areas were reached. All specimens were evaluated for histomorphometry, and samples were stained using hematoxylin and eosin (HE) staining methods.

3. Results and discussion

3.1. Characterization of the JEM(+)/JEM(−) membrane

P(VDF-TrFE), a copolymer of PVDF, that possesses the desired electroactive β phase was fabricated via a solution casting method (Fig. 1a). X-ray diffraction (XRD) patterns indicated that the P(VDF-TrFE) membrane contained a high β phase content (Fig. 1b), and thus was expected to exhibit an increased piezoelectric response. The hydrophilicity of the JEM membranes was also tested (Fig. S1). The differences in water contact angle were not significant between the groups. Tensile strength and the elastic modulus of JEM membranes decreased compared with the control group. (Fig. S3). According to a previous study, the tensile strength and elastic modulus changes on this scale will not affect osteogenesis [30]. The polarization-electric field (P-E) hysteresis loop at room temperature of the JEM membrane showed that the P(VDF-TrFE) membrane used for preparing the JEM membrane exhibited an oval-shaped loop with a relatively low-intensity electric field, indicating the good polarization properties of the membrane (Fig. S2). We also performed electric polarization to direct the electric dipole to induce different surface potentials on different sides of the P(VDF-TrFE) membrane. Analysis of the piezoelectric constant d_{33} suggested that the P(VDF-TrFE) membrane was polarized with an equal absolute d_{33} value (d_{33} = 10.48 ± 1.28 pC/N) on either side. The remnant polarization of the P(VDF-TrFE) membranes ensured the transition of the surface potential. SKPFM was used to characterize the surface potential of both sides of the polarized P(VDF-TrFE) membrane, and the results indicated that the surface potential of the positively polarized surface (JEM(+)) was more than 240 mV higher than that of the negatively polarized surface (JEM(−)) (Fig. 1c and d). These results confirmed the development of appropriately charged surfaces on the JEM membrane. To test the piezoelectric stability of the membranes, they were immersed in Dulbecco's modified Eagle's medium solution for 30 days. A d_{33} value of 9.51 ± 0.64 pC/N was recorded for the immersed samples at the end of 30 days, which is close to the original d_{33} value.

3.2. Cell viability on either side of the JEM membrane

Cell viability was measured to assess the difference in cytocompatibility between the two sides of the JEM membrane. rBMSCs and hGFs were co-cultured with the JEM membrane, respectively. The cell

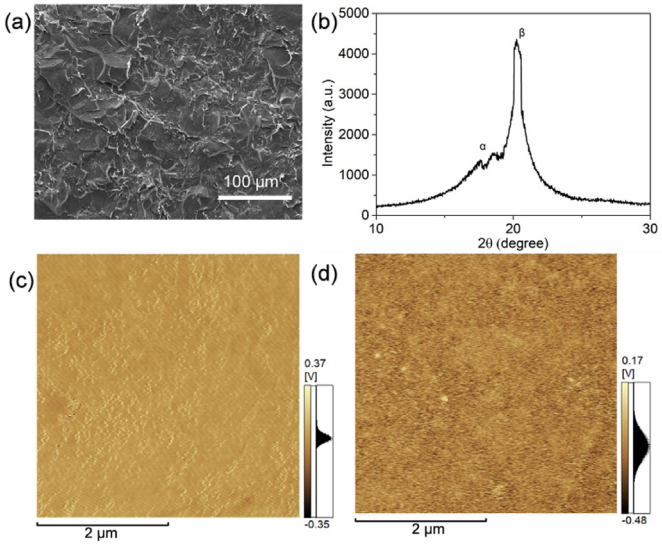

Fig. 1. Characterization of the JEM membranes. (a) SEM image and (b) XRD patterns of the P(VDF-TrFE) membranes. (c, d) SKPFM surface potential image of the positively and negatively polarized sides of the P(VDF-TrFE) membranes.

counting kit 8 (CCK-8) assay (Fig. 2a) and lactate dehydrogenase (LDH) assay (Fig. S4) were used to evaluate the biocompatibility of the JEM membranes. The results showed no significant difference in LDH activity between the JEM membrane and the control membrane on rBMSCs and hGFs. In the CCK8 assay, the proliferation rate of rBMSCs was higher for cells cultured on the JEM(−), whereas the proliferation rate of hGFs was higher for cells cultured on the JEM(+) at 3 and 5 days. These results show that the polarized JEM membranes promoted cell proliferation. The JEM(−) promoted rBMSC proliferation better, whereas the JEM(+) promoted hGFs proliferation better.

Cell morphology represents the cell growth and spreads status. Therefore, cytoskeleton and nuclear staining were performed on rBMSCs and hGFs on the JEM(−) and JEM(+) and control membranes to observe differences in cell morphology. The images of the cytoskeleton (Fig. 2b) showed that rBMSCs cultured on the JEM(−) had an extended morphology and increased cell surface area compared with those cultured on the JEM(+) or control membranes. However, gingival fibroblasts cultured on the JEM(+) membrane showed a better and more intensive spread than those cultured on the JEM(−) or control membranes. Cell morphology and function are closely related [31]. Therefore, rBMSCs on the JEM(−) membrane and hGFs on the JEM(+) membrane may have better biofunctions.

3.3. In vitro osteogenic differentiation on the JEM membrane

ALP activity and mineral deposition assays were performed to study the osteogenic performance of rBMSCs cultured on the JEM membranes (Fig. 3a). Massive blue-stained aggregates representing ALP were detected on both JEM(−) and JEM(+) membranes at 7 days, but were more apparent on the JEM(−) membrane. Alizarin red staining showed that rBMSCs cultured on the JEM(−) membrane secreted larger amounts of mineralization nodules than those cultured on the JEM(+) and control membranes at 21 days (Fig. 3a). Quantitative results of ALP and alizarin red staining results indicated that the ALP activity and mineralization of rBMSCs cultured on the JEM(−) membrane were the highest among the three groups (Fig. 3b and c). The expression of osteogenic genes, including *Runx2, Ocn, ColI,* and *Opn,* was also evaluated (Fig. 3d). *Runx2* expression was measured at 3 and 7 days, and *Ocn, Opn,* and *ColI* expression were measured at 14 and 21 days. The results showed that the transcription levels of *Runx2* cells on both JEM(−) and JEM(+) membranes were upregulated, but were higher on the JEM(−) than on the JEM(+) membranes. *Ocn, Col I,* and *Opn* were upregulated on the JEM(−) membrane, whereas the difference in expression levels between JEM(+) and control membranes was not significant (Fig. 3d). Protein expression results (Fig. 3e and f) showed that RUNX2, OCN, COL I, and OPN were highly expressed in cells cultured on the JEM(−) membrane at 14 days. In addition, the expression levels of OPN and OCN on the JEM(+) membrane were higher than those on the control membranes but lower than those on the JEM(−) membrane. Both gene and protein levels indicated that JEM(−) effectively promoted the osteogenic differentiation of rBMSCs, whereas only a few osteogenic indices of JEM(+) were upregulated, indicating that JEM(−) is better than JEM(+) for bone regeneration. These results confirmed that the osteogenic performance of GBR membranes can be regulated via the electric microenvironment, which is consistent with a previous study [30,32,33].

3.4. In vitro hGFs migration efficiency on the JEM membranes

Next, we evaluated the effect of the JEM membranes on hGFs behavior, which is closely related to soft tissue healing. During the period of tissue healing, fibroblasts first migrate to the wound, and then proliferate and differentiate to repair damaged tissue [13,15,16]. Thus, to further study which side of the JEM membrane promotes soft tissue healing better, a transwell assay was carried out to analyze hGFs migration on the JEM membranes. The migratory ability of hGFs on the JEM(+) membrane was better than that on the JEM(−) and control membranes (Fig. 4a and b, Fig. S5).

Studies have shown that cell migration is affected by many factors, including signal transduction, the cytoskeleton, and focal adhesions [34]. FAK is a tyrosine-protein kinase that plays an important role in signal transduction and acts as a central node of the integrin signaling axis, regulating the formation of focal adhesions during cell migration [35]. Fibronectin is a macromolecular glycoprotein that is a key substance that promotes wound healing. Col I makes up the extracellular matrix and participates in cell migration. Therefore, PCR was used to detect the transcription levels of migration-related genes (*Fak, Fn1, and Col I*). The

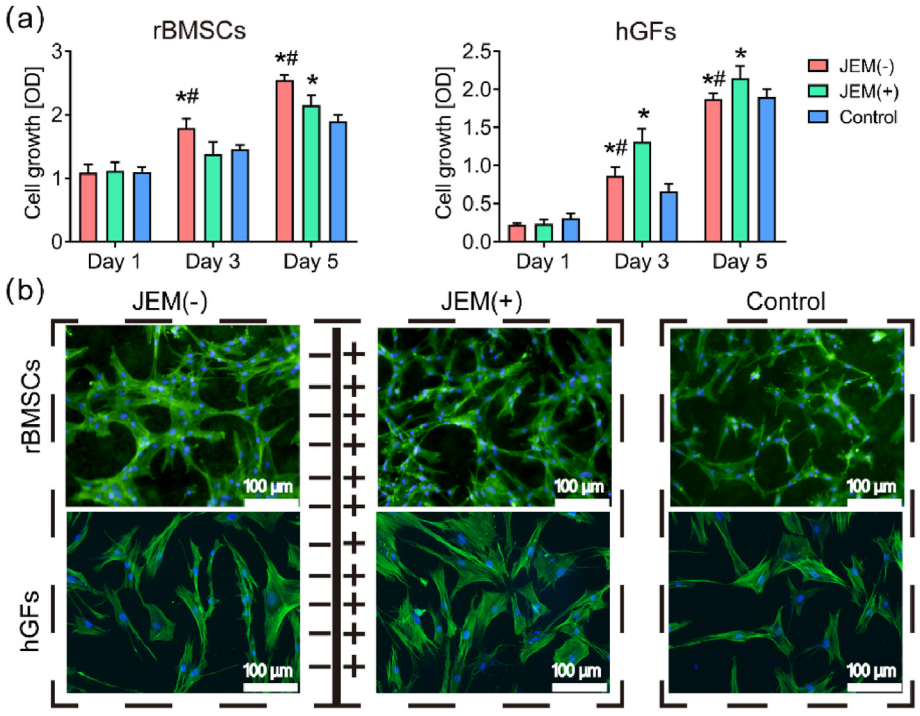

Fig. 2. Biocompatibility of rBMSCs and hGFs on the JEM membrane. (a) CCK8 assay for rBMSCs and hGFs grown on JEM(+), JEM(−), and control membranes at 1, 3, and 5 days, n = 6. (b) Immunofluorescence images of the cytoskeletal network (phalloidin, green) and nuclei (DAPI, blue) of rBMSCs and hGFs on JEM(+), JEM(−), and control membranes at 3 days. The scale bar in b is 100 μm *p < 0.05, compared with Control; #p < 0.05, compared with JEM(+). Statistically significant differences (p < 0.05) were measured using a one-way analysis of variance (ANOVA) combined with the Student–Newman–Keuls (SNK) multiple comparison post hoc test.

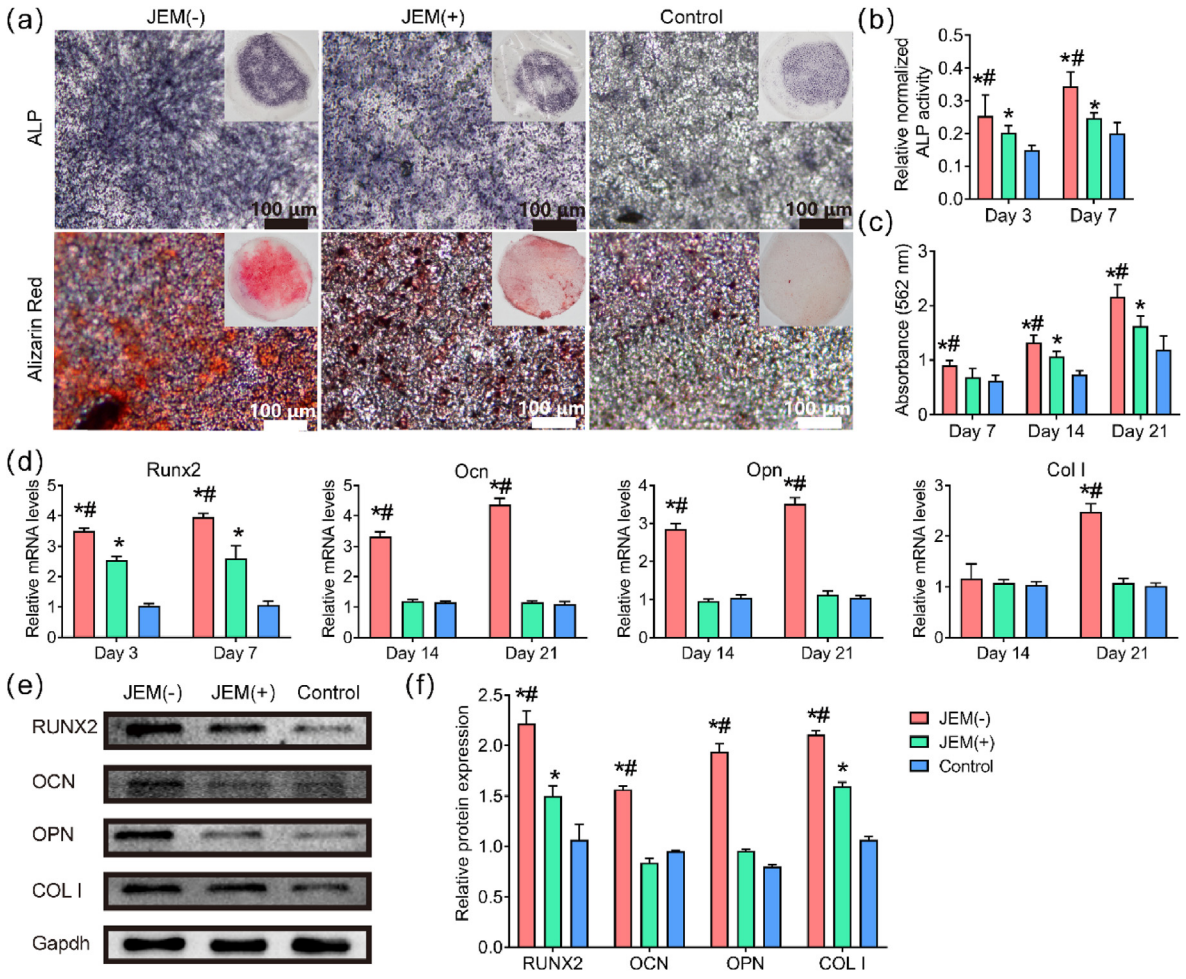

Fig. 3. Evaluation of osteogenesis in rBMSCs grown on JEM membranes. (a) Images of ALP staining (blue) and Alizarin red staining (red) of rBMSCs at 7 and 21 days. Insets show macroscopic images. The scale bar in (a) is 100 μm. (b and c) Quantitative analysis of ALP activity and Alizarin red staining, n = 6. (d) qRT-PCR analysis of osteogenesis-related gene expression (*Runx2*, *Ocn*, *ColI*, and *Opn*) in rBMSCs on JEM(+), JEM(−), and control membranes at the indicated days, n = 9. (e and f) Western blot of osteogenesis-related proteins in rBMSCs on JEM(+), JEM(−), and control membranes at 14 days, n = 6. *p < 0.05, compared with Control; #p < 0.05, compared with JEM(+). Statistically significant differences (p < 0.05) were measured using a one-way analysis of variance (ANOVA) combined with the Student–Newman–Keuls (SNK) multiple comparison post hoc test.

results showed that the transcription levels of *FAK, FN1* and *COLI* were upregulated in hGFs on the JEM(+) membrane at 24 h (Fig. 4c). Western blot results also showed that FAK, FN1, and COLI were highly expressed on the JEM(+) membrane at 24 h (Fig. 4d). The above results show that the JEM(+) membrane can better increase cell migration. The osteogenic and migration results confirm that the JEM membrane provides different electric microenvironments on either side to promote bone regeneration and wound healing, which is expected to realize surface-selective osteogenesis/gingival healing performance for GBR.

3.5. *In vivo* bone regeneration by the JEM membranes

To verify the effects of the JEM membrane on bone defects *in vivo*, 6-week-old SD rats (180 ± 20 g, male) with freshly formed critical-sized round mandibular defects (4 mm diameter) were surgically implanted with JEM(+), JEM(−), and control membranes (Fig. S6). Bone growth was evaluated at 4 and 8 weeks after implantation. At 4 weeks, as evidenced by micro-CT detection, the edge of the defects was filled with new bone, and a small area in the middle of the defects was left empty when covered with the JEM(−) membrane; similarly, a small empty area existed when covered with the JEM(+) membrane. When using the control membrane, a large area was exposed in the middle of the defects and a small amount of new bone was formed on the edge of the defect. At 8 weeks, the defect was filled with a homogeneous and consecutive regenerated mature bone when covered with the JEM(−) membrane, but a small empty area still existed in the middle of the defects when covered with the JEM(+) membrane, and a large empty area was still exposed when covered with the control membrane (Fig. 5a). The values of bone volume/total volume (BV/TV, %), which reflect the quantity of the new bone formed, were higher in the JEM(−) group than in the other groups after 4 and 8 weeks (Fig. 5b).

H&E staining was performed to further study the newly formed bone. As shown in Fig. 5c, the new trabecular bone was thicker, the bone marrow cavity formation was irregular, and the fibrous connective tissue was thin when covered with the JEM(−) membrane for 4 weeks. By contrast, in the JEM(+) group, the new trabecular bone was relatively small, and the fibrous connective tissue was thicker; in the control group, the fibrous connective tissue occupied the bone defect and few new bone formations were observed after 4 weeks. At 8 weeks post-surgery, the new bone almost covered the entire bone defect area in the JEM(−) group, with the new bone having lamellar collagen fibers and the presence of osteocytes in lacunae, indicating a compact bone; moreover, few fibrous connective tissues were visible. In the JEM(+) group, new bone formation and thin fibrous connective tissue were observed. In the control group, abundant fibrous tissue occupied the defect area, and very few new trabecular bones formed a reticular structure with substantial

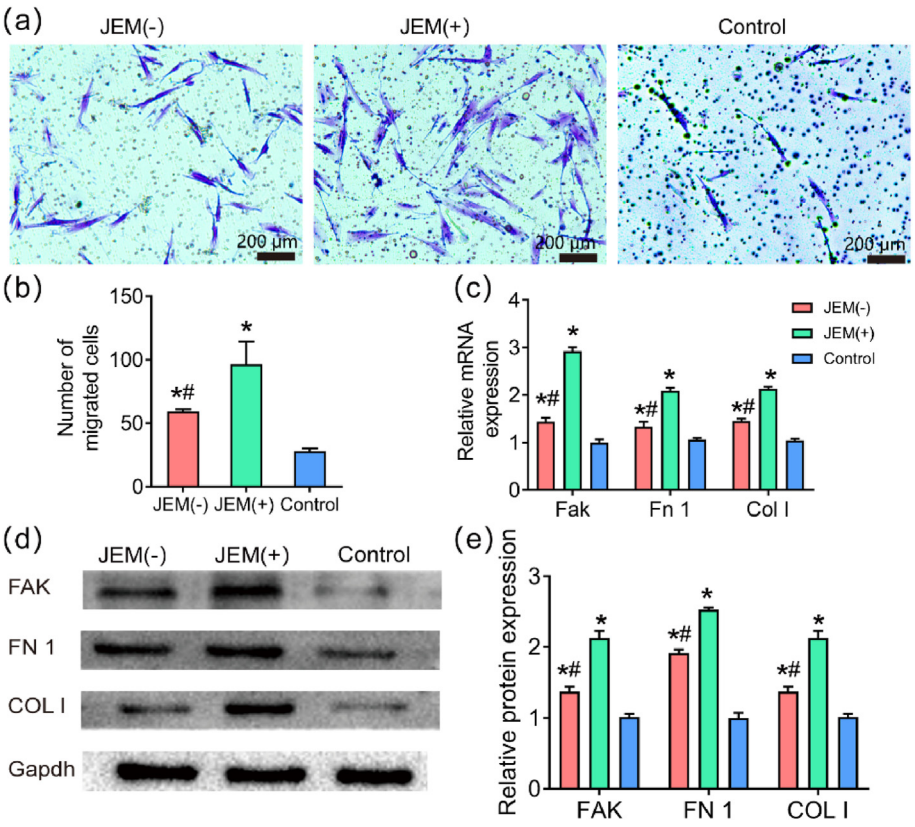

Fig. 4. Cell migration of hGFs on JEM membranes. (a and b) Representative images and quantitative analysis of hGFs on JEM(+), JEM(−), and control membranes at 24 h in the transwell assay. The scale bar in a is 200 μm, n = 6. (c) qRT-PCR analysis of migration-related gene expression (*FAK*, *FN1*, and COLI), n = 9. (d and e) Western blot analysis of migration-related proteins (FAK, FN1, and COL I) in hGFs on JEM(+), JEM(−), and control membranes at 24 h, n = 6. *p < 0.05, compared with Control; #p < 0.05, compared with JEM(+). Statistically significant differences (p < 0.05) were measured using a one-way analysis of variance (ANOVA) combined with the Student–Newman–Keuls (SNK) multiple comparison post hoc test.

interspace. These results indicate that JEM(+)/JEM(−)-composite membranes can trigger fast bone repair processes because of their electro-microenvironment and that the JEM(−) membrane has the strongest effect on osteogenesis (Fig. 5c). Biomaterial-mediated immune response is a critical factor to determine the cell fate as well as the tissue-regenerative outcome [26,36]. Results shown that the inflammatory reaction of electro-microenvironment are slight compared to control group (Fig. 5c). A Study showed that when the polarized membrane is covering the bone defect area, the polarized materials created a favorable osteo-immunomodulatory environment, thus promoting osteogenic differentiation [37]. Our study shown the same results that the JEM(−) membrane effectively promoted the osteogenic differentiation of rBMSCs *in vitro* and the bone defect was filled with homogeneous and consecutive regenerated mature bone *in vivo*. This might be relate to biomaterial-mediated immune response, the mechanism still needs to be explored. Overall, bone defect healing was significantly improved after treatment with the JEM(−) membrane, which is consistent with the results of the *in vitro* osteogenic experiment. This can be attributed to the electro-microenvironment-regulated proliferation and differentiation of rBMSCs.

3.6. *In vivo* gingival healing by the JEM membranes

To verify the gingival healing ability of the JEM membranes *in vivo*, rat palatal wounds (3 mm diameter) were surgically covered with either JEM(+) or JEM(−) membrane. The rats were euthanized on days 7, 14, and 21. Evaluation of the wound surface area was performed using ImageJ. The result showed that the palatal wounds of the controls and rats implanted with JEM showed no physiological abnormalities during the experiment. The wound surface area visually indicated that the palatal wounds of the controls and rats implanted with JEM showed no physiological abnormalities during the experiment. The wound surface area was not completely epithelized on day 7 and was readily distinguished from the undamaged intact tissue that was pale pink in color (Fig. 6a). Further statistical analysis showed that the wound surface area of the JEM(+) group was smaller than that of the JEM(−) and control groups on day 7 (Fig. 6b). On day 14, the wounds in the JEM(+) group were covered by epithelium, and the central depression was smaller than that in the JEM(−) and control groups (Fig. 6a). Again, the wound surface area of the JEM(+) group was smaller than that of the JEM(−) and control groups (Fig. 6b). On day 21, the wounds in the JEM(+) group were completely healed and flattened, whereas those in the JEM(−) group were not completely flattened. The surface mucosa of the control group was thin and sunken (Fig. 6a). There were no significant differences in the wound healing area among the three groups (Fig. 6b).

Finally, we observed the new tissue formed above the JEM membrane and measured the maximum distance of the non-epithelialized area in H&E-stained sections (Fig. 6d). On day 7, the width of the wound in the JEM(+) group was significantly reduced and the wound tissue showed densely granulated structure accompanied by the proliferation of capillaries and an increase in the number of fibroblasts. In the JEM(−) group, the new tissue was disordered and loosely granulated, whereas the control group had less newly granulated tissue overall (Fig. 6d and Fig. S7a). On day 14, in the JEM(+) group, the wound was healed with the formation of stratified squamous epithelium, which was slightly parakeratotic with numerous rete pegs. Beneath the epithelium, the collagen fiber network was coarse. By contrast, the fibrous tissue was less dense, the collagen bundles were thinner, and the rete pegs were smaller in the JEM(+) group than in the JEM(−) group. The control wound showed a disordered cellular arrangement and was still not completely healed. By day 21, the wounds in the three groups had healed, and collagen fibers in the submucosa increased in number and were arranged in thicker bundles in the JEM(+) and JEM(−) groups. However, in the control group, the fibrous tissue was less dense, and the collagen bundles were thinner (Fig. 6d and Fig. S7a). The difference in the maximum width of the non-epithelialized area at each time point was significant during the experiment for each of the three groups. The maximum healing width of the non-epithelial area in the JEM(+) group was the

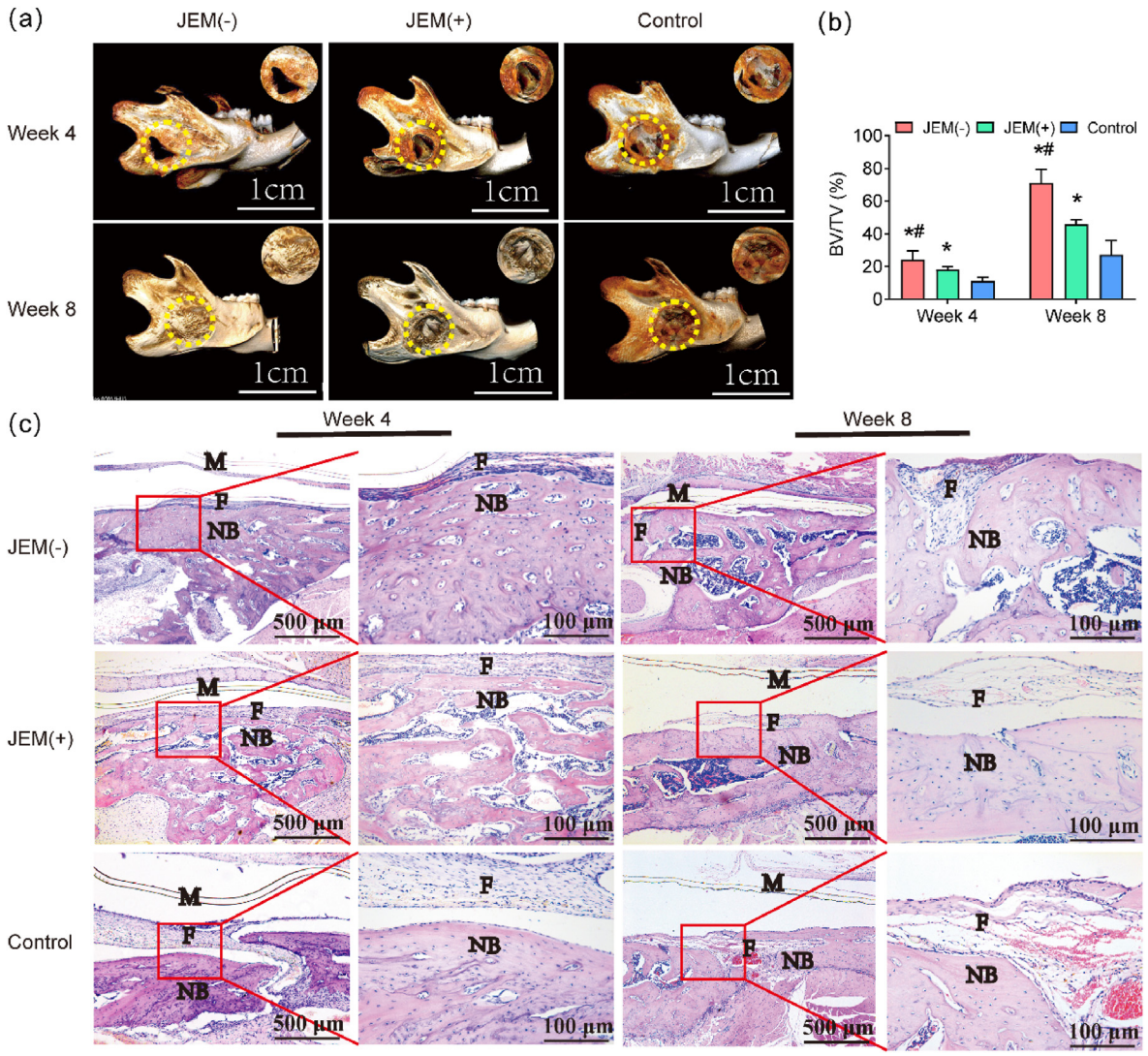

Fig. 5. *In vivo* bone defect repair experiment using a rat model of mandibular defect implanted with JEM membrane. (a) Reconstructed micro-CT images of critical-sized rat mandibular defects at 4 and 8 weeks of JEM membrane implantation. Yellow dotted lines denote the original bone defect. The scale bar in a is 1 cm. (b) Quantitative analysis of bone volume/total volume (BV/TV), n = 3. (c) Histological analysis of newly regenerated bone 4 and 8 weeks after implantation of JEM using H&E staining. The scale bar in c is 100 μm and 500 μm. M, membrane; F, fibrous tissue; NB, osteoid tissue. All scale bars in c correspond to 100 or 500 μm *$p < 0.05$, compared with Control; #$p < 0.05$, compared with JEM(+). Statistically significant differences ($p < 0.05$) were measured using a one-way analysis of variance (ANOVA) combined with the Student–Newman–Keuls (SNK) multiple comparison post hoc test.

smallest, and healing was the fastest ($p < 0.05$). This is consistent with the results of the *in vitro* studies. Thus, the *in vivo* rat palatal wound healing model also demonstrated that the JEM(+) membrane promotes soft tissue healing. Overall, the above results show that, as hypothesized, the JEM(−) membrane promotes bone regeneration and that the JEM(+) membrane promotes soft tissue healing.

3.7. Effect of electro-microenvironment on bone regeneration

We have shown that the JEM(−) membrane effectively promotes the osteogenic differentiation and mineralization of rBMSCs *in vitro* and mandible bone defect healing *in vivo*. A previous study has shown that the electrical microenvironment regulates the MMP [32], changes that are closely related to the deposition of calcium phosphate minerals triggered by mitophagy. Mitophagy is involved in developmental processes that require mitochondrial clearance, and its impairment drastically alters mitochondrial function and cell fate in many cell types [11]. Although augmented autophagic flux has been identified during osteoblast differentiation and mineral nodule formation [38], the role of mitophagy in osteogenesis promoted by an electro-microenvironment remains unclear. The MMP of rBMSCs cultured on the JEM(−) membrane for 7 days showed the highest degree of depolarization, followed by that of those on the JEM(+) membrane (Fig. S8). Flow cytometry also showed that the MMP of cells cultured on the JEM(−) membrane was highly depolarized (Fig. 7a and b). We further investigated autophagy-related genes and proteins. LC3 is a specific marker of autophagosome formation. The expression of LC3 increased most notably on the JEM(−) membrane (Fig. 7c). The PCR results (Fig. 7c) showed an upregulation in the transcription levels of *LC3*, *Pink I*, and *Parkin* on the JEM(−) membrane at 3, 5, and 7 days. Conversely, on the JEM(+) membrane, only the expression of the *LC3* gene was upregulated, and that of the *Pink I* and *Parkin* genes was not significantly different from that in the control group. PINK1 is a key factor for initiating mitophagy, and the PARKIN signal is required for mitophagy induction by ubiquitinating mitochondrial proteins [15]. The results above indicated that the JEM(−) membrane may activate mitophagy. Activation of the Pink I/Parkin pathway induces mitochondrial autophagocytosis, followed by lysosomal digestion and finally the release of calcium phosphate to the extracellular matrix to promote bone

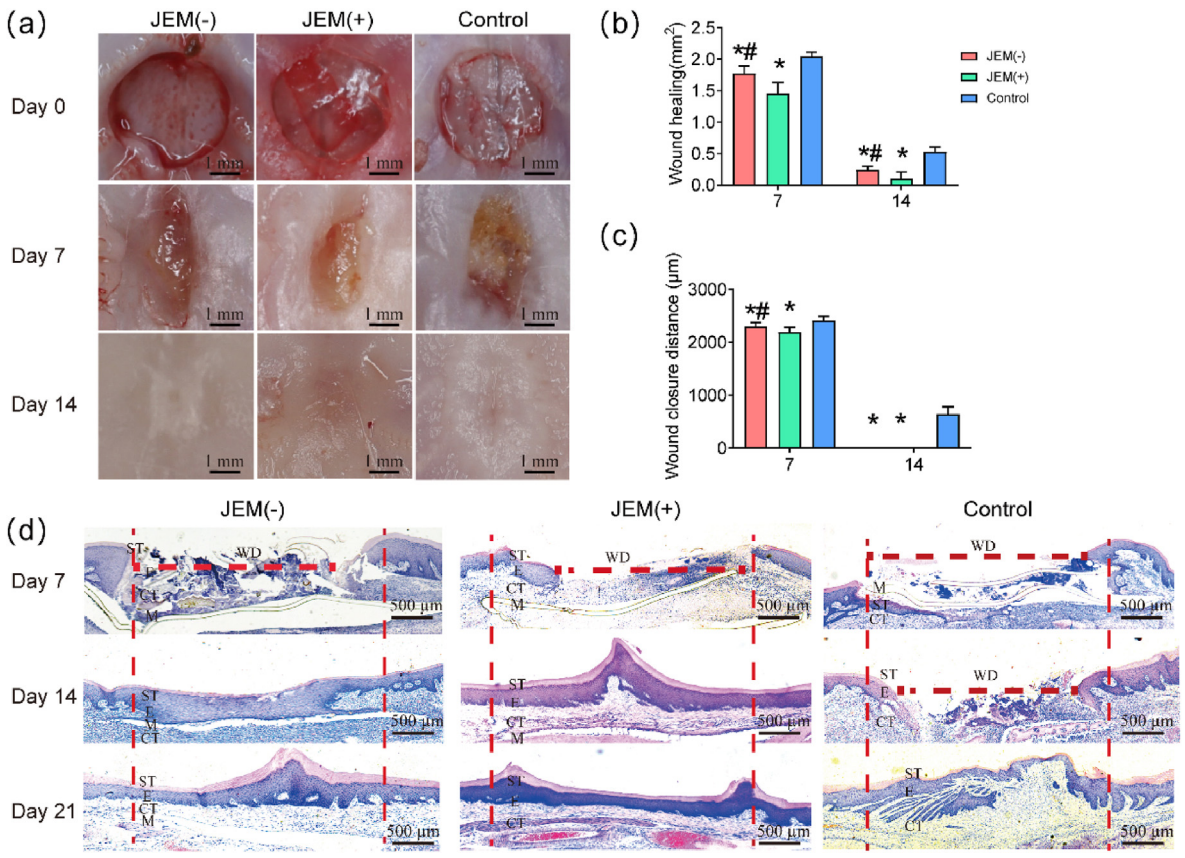

Fig. 6. *In vivo* soft tissue defect repair experiment using a rat model of palatal wounds implanted with JEM membrane. (a) Optical microscopic images of palatal wound healing after JEM membrane implantation. The scale bar in a is 1 mm. (b) Quantitative analysis of the wound surface healing area after JEM membrane implantation, n = 3. (c) Quantitative analysis of mucosa wound closure distance after JEM membrane implantation, n = 3. (d) Histological analysis of newly regenerated soft tissue after JEM implantation using H&E staining. The scale bar in c is 500 μm. ST, stratum corneum; E, epithelium; CT, connective tissue; M, membrane; WD, wound distance. *p < 0.05, compared with Control; #p < 0.05, compared with JEM(+). Statistically significant differences (p < 0.05) were measured using a one-way analysis of variance (ANOVA) combined with the Student–Newman–Keuls (SNK) multiple comparison post hoc test.

mineralization [39]. Therefore, the osteogenic efficiency of the JEM(−) membrane was possibly enhanced by the activation of mitochondrial autophagy.

3.8. Effect of electro-microenvironment on gingival healing

We have shown that the JEM(+) membrane promotes hGFs migration *in vitro* and rat palatal gingival healing *in vivo*. Healing is a complex, high-energy-demand metabolic process. Mitochondria are the main cellular organelles that provide energy for metabolism and biosynthesis through the production of ATP. Studies have shown that ATP is produced through mitochondrial oxidative phosphorylation (OXPHOS) to support functions involved in cellular migration, such as adhesion, proliferation, and differentiation [40] To explore the mechanism activated by the electro-microenvironment during wound healing, we focused on the effect of the electro-microenvironment on fibroblast ATP production. We used the Seahorse Bioscience XF24 analyzer to evaluate the effect of the JEM membranes on OXPHOS using the oxygen consumption rate (OCR) as a marker. The OCR and measurement time(plot) showed that the JEM(+) membrane increased OCR in hGFs. The basal respiration rate was measured in hGFs on JEM(+), JEM(−), and control membranes, and then oligomycin, FCCP, and rotenone were added to detect changes in OCR at various stages (Fig. 8a). The results showed that the JEM(+) membrane increased basal respiration (Fig. 8b), maximum respiration (Fig. 8c), proton leakage (Fig. 8d), ATP production (Fig. 8e), spare respiration (Fig. 8f), and mitochondrial respiration (Fig. 8g) compared to those by the JEM(−) and control membranes. OXPHOS occurs primarily in the inner membrane of mitochondria and is dependent on the electron transport chain. The main components of the electron transport chain are complexes I, II, III, IV, and V, which maintain mitochondrial energy production through a stable proton gradient. Thus, we investigated the protein expression of complexes I–V. Western blots showed an increased protein expression in hGFs on the JEM(+) membrane at 24 h (Fig. 8i). According to these results, the JEM(+) membrane promotes mitochondrial OXPHOS, which provides energy for fibroblast metabolism and biosynthesis, thereby supporting fibroblast migration and proliferation and finally promoting wound healing (Fig. 8j).

The JEM(−) membrane promoted osteogenic differentiation and mineralization, which may be related to mitophagy. The JEM(+) membrane promoted the proliferation and migration of hGFs, which may be related to an acceleration of mitochondrial energy metabolism. Compared with the clinical membrane, this double-sided hetero-electric membrane constructs the electrical microenvironment using built-in localized electrical stimuli. This electrical characteristic might regulate mitochondrial autophagy and energy metabolism, and then promote bone regeneration and closure of soft tissue wounds.

4. Conclusion

One of the critical problems of GBR membranes is the ability to reach a favorable balance between bone regeneration and gingival healing from the perspective of bionics, particularly when faced with severe bone defects. Only recently have we come to realize the significance of addressing JEM in the GBR process. However, to apply this concept toward effective treatment, the ability to combine built-in localized electrical stimuli with precise spatial control and long durability is required.

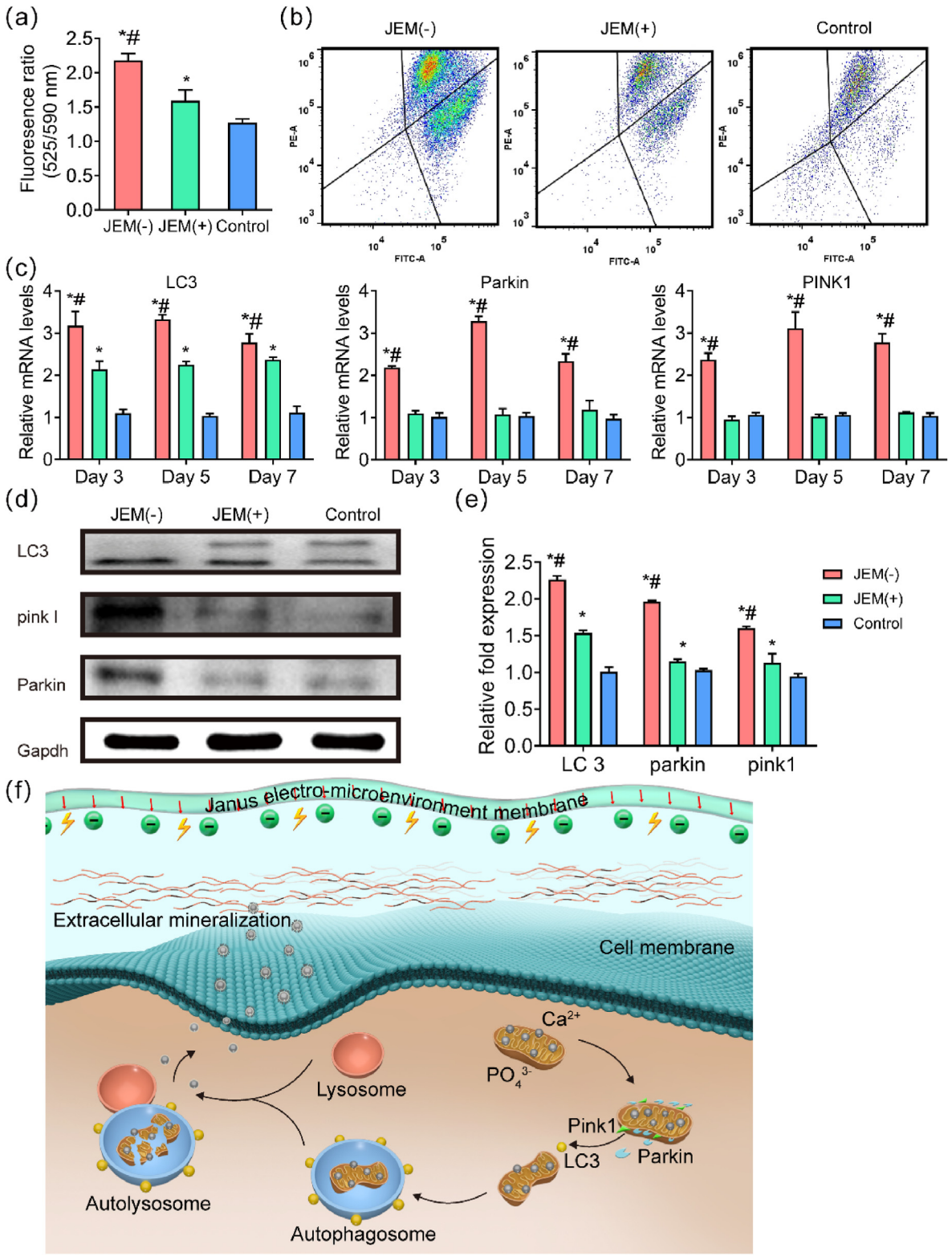

Fig. 7. Evaluation of mitophagy in rBMSCs on JEM membranes. (a and b) Quantitative analysis of changes in mitochondrial membrane potential in rBMSCs at 7 days, n = 6. (c) qRT-PCR analysis of mitophagy-related gene expression (*LC3* II, *Pink I*, and *Parkin*) in rBMSCs on JEM(+), JEM(−), and control membranes at 3, 5, and 7 days, n = 9. (d and e) Western blot of mitophagy-related proteins (LC3 II, PINK I, and PARKIN) in rBMSCs on JEM(+), JEM(−), and control membranes at 14 days, n = 6. (f) Schematic illustration of mitophagy induced by the JEM(−) membrane. When the JEM(−) membrane interacts with rBMSCs, the mitochondria swell and lose their membrane potential, activating PINK1-PARKIN-mediated mitophagy. The damaged mitochondria are digested by autolysosomes and release intramitochondrial mineral particles into the extracellular matrix, which promotes mineralization. *p < 0.05, compared with Control; #p < 0.05, compared with JEM(+). Statistically significant differences (p < 0.05) were measured using a one-way analysis of variance (ANOVA) combined with the Student–Newman–Keuls (SNK) multiple comparison post hoc test.

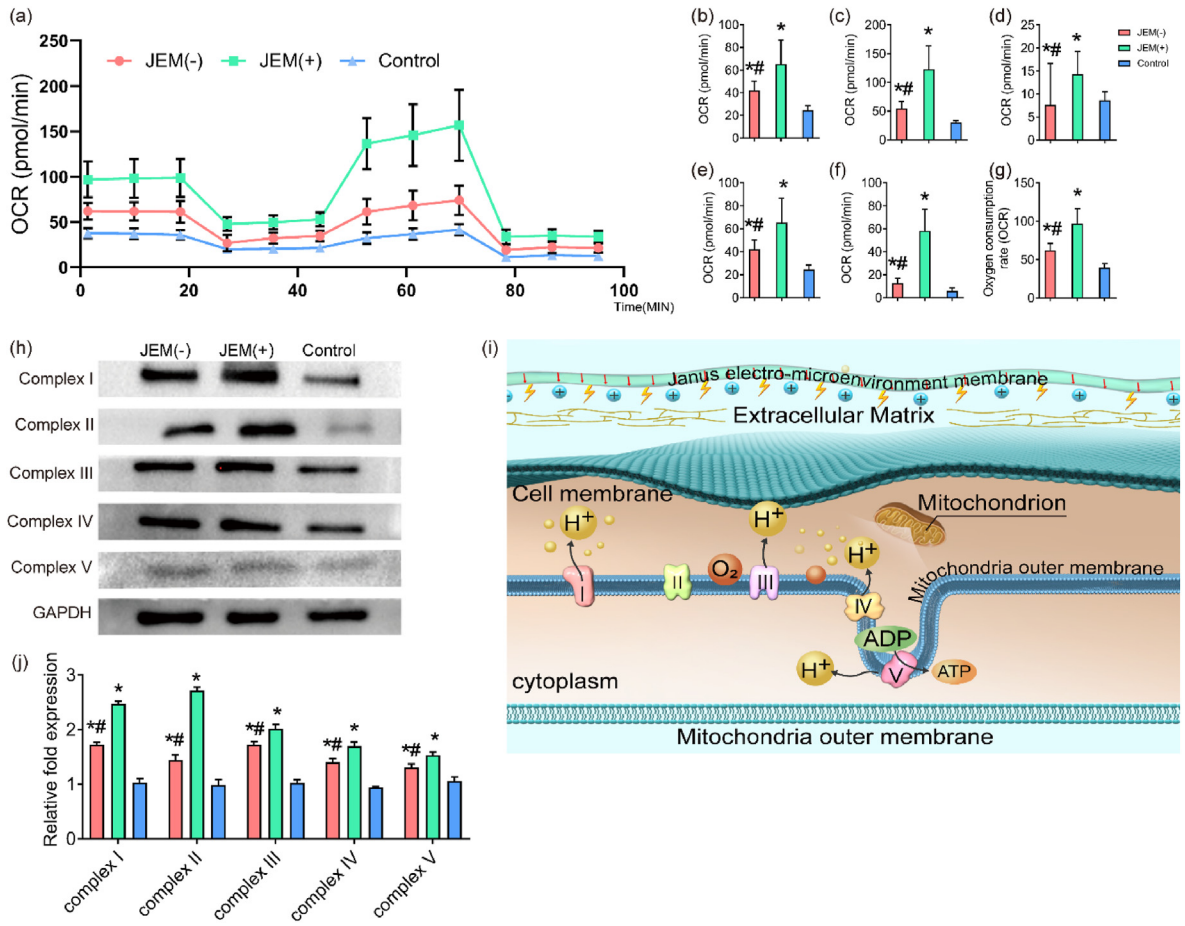

Fig. 8. Evaluation of mitochondrial oxidative phosphorylation (OXPHOS) in hGFs grown on JEM membranes. (a) Time course (min) and oxygen consumption rate (OCR) curve plot for hGFs on JEM(+), JEM(−), and control membranes. hGFs were examined using the Seahorse Bioscience XF24. Quantification was performed for additional parameters, including (b) basal respiration, (c) maximal respiration, (d) proton leak, (e) ATP production, (f) spare respiration proton leak, and (g) mitochondrial respiration. (h and i) Western blot of mitochondrial proteins related to OXPHOS (Complexes I, II, III, IV, and V) in hGFs cultured on JEM(+), JEM(−), and control membranes at 24 h. (j) Schematic illustration of mitochondrial OXPHOS in hGFs grown on the JEM(+) membrane. When the JEM(+) membrane acts on hGFs, OXPHOS increases and the electron transport chain in the mitochondrial inner membrane is activated. This metabolic pathway drives the synthesis and release of ATP as an energy source, which is expected to promote the proliferation and migration of hGFs. *$p < 0.05$, compared with Control; #$p < 0.05$, compared with JEM(+). Statistically significant differences ($p < 0.05$) were measured using a one-way analysis of variance (ANOVA) combined with the Student–Newman–Keuls (SNK) multiple comparison post hoc test, $n = 3$.

In this study, we successfully constructed a JEM membrane using the casting and polarization method. Owing to the heterogeneity of the electro-microenvironment on the two sides of the membrane-tissue interface, the JEM membrane could represent a fast and controlled tool to promote both bone and soft tissue healing. The JEM(−) membrane effectively promoted the osteogenic differentiation of rBMSCs, which was demonstrated to be related to the stimulation of mitochondrial autophagy. The JEM(+) membrane effectively enhanced the proliferation, migration, and differentiation of hGFs, which was demonstrated to be related to increased mitochondrial OXPHOS. Therefore, such a bifunctional barrier membrane, with varied and opposite electrophysiological microenvironments of the two interfaces, that integrates bone regeneration with wound healing could provide a promising clinical strategy for oral implant therapy in the future, along with an important guideline for future interface material design.

This study still has some limitations. For example, P(VDF-TrFE) needs to improve hydrophilicity and porosity, which are important properties of implanted materials. Moreover, further experiments are needed to verify the mechanism of the electro-microenvironment.

Credit author statement

C. Lai and C. Ning: experiment design. Z. Zhou and Z. Yi: constructed P(VDF-TrFE) and performed material analysis. P. Zhu, Y. Xu, and Y. He: performed the animal experiment M. Cheng: performed the cell experiment and evaluated the data. P. Yu and S. XU: supervised this study. C. Lai and P. Yu wrote the paper.

Declaration of competing interest

The authors declare that they have no known competing financial interests or personal relationships that could have appeared to influence the work reported in this paper.

The authors declare that they have no known competing financial interests or personal relationships that could have appeared to influence the work reported in this paper.

Data availability

The authors are unable or have chosen not to specify which data has been used.

Acknowledgements

The authors acknowledge the financial support for this work from the National Natural Science Foundation of China (No. 52072127, No. 52003085) and the China Postdoctoral Science Foundation. (No. 2020M672642).

Appendix A. Supplementary data

Supplementary data to this article can be found online at https://doi.org/10.1016/j.mtbio.2022.100491.

References

[1] T.E. Lindley, N.S. Dahdaleh, A.H. Menezes, K.O. Abode-Iyamah, Complications associated with recombinant human bone morphogenetic protein use in pediatric craniocervical arthrodesis, J. Neurosurg. Pediatr. 7 (2011) 468–474.
[2] I. Elgali, O. Omar, C. Dahlin, P. Thomsen, Guided bone regeneration: materials and biological mechanisms revisited, Eur. J. Oral Sci. 125 (2017) 315–337.
[3] D.S. Thoma, S.P. Bienz, E. Figuero, R.E. Jung, I. Sanz-Martín, Efficacy of lateral bone augmentation performed simultaneously with dental implant placement: a systematic review and meta-analysis, J. Clin. Periodontol. 46 (21) (2019) 257–276.
[4] J. Liu, D.G. Kerns, Mechanisms of guided bone regeneration: a review, Open Dent. J. 8 (2014) 56–65.
[5] B. Feng, S. Wang, D. Hu, W. Fu, J. Wu, H. Hong, I.J. Domian, F. Li, J. Liu, Bioresorbable electrospun gelatin/polycaprolactone nanofibrous membrane as a barrier to prevent cardiac postoperative adhesion, Acta Biomater. 83 (2019) 211–220.
[6] T. Jiang, E.J. Carbone, K.W.H. Lo, C.T. Laurencin, Electrospinning of polymer nanofibers for tissue regeneration, Prog. Polym. Sci. 46 (2015) 1–24.
[7] C. Ning, Z. Zhou, G. Tan, Y. Zhu, C. Mao, Electroactive polymers for tissue regeneration: developments and perspectives, Prog. Polym. Sci. 81 (2018) 144–162.
[8] M. Levin, Bioelectric signaling: reprogrammable circuits underlying embryogenesis, regeneration, and cancer, Cell 184 (2021) 1971–1989.
[9] H. Palza, P.A. Zapata, C. Angulo-Pineda, Electroactive smart polymers for biomedical applications, Materials 12 (2019).
[10] H.B. Murray, B.A. Pethica, A follow-up study of the in-practice results of pulsed electromagnetic field therapy in the management of nonunion fractures, Orthop. Res. Rev. 8 (2016) 67–72.
[11] I.S. Aleem, I. Aleem, N. Evaniew, J.W. Busse, M. Yaszemski, A. Agarwal, T. Einhorn, M. Bhandari, Efficacy of electrical stimulators for bone healing: a meta-analysis of randomized sham-controlled trials, Sci. Rep. 6 (2016), 31724.
[12] E.B. Nguyen, J. Wishner, K. Slowinska, The effect of pulsed electric field on expression of ECM proteins: collagen, elastin, and MMP1 in human dermal fibroblasts, J. Electroanal. Chem. 812 (2018) 265–272.
[13] Y. Wang, M. Rouabhia, Z. Zhang, Pulsed electrical stimulation benefits wound healing by activating skin fibroblasts through the TGFβ1/ERK/NF-κB axis, Biochim. Biophys. Acta 1860 (2016) 1551–1559.
[14] B.C. Heng, Y. Bai, X. Li, Y. Meng, X. Zhang, X. Deng, Signaling pathways implicated in enhanced stem/progenitor cell differentiation on electroactive scaffolds, Smart Materials in Medicine 3 (2022) 4–11.
[15] B. Tandon, J.J. Blaker, S.H. Cartmell, Piezoelectric materials as stimulatory biomedical materials and scaffolds for bone repair, Acta Biomater. 73 (2018) 1–20.
[16] C. Ning, P. Yu, Y. Zhu, M. Yao, X. Zhu, X. Wang, Z. Lin, W. Li, S. Wang, G. Tan, Y. Zhang, Y. Wang, C. Mao, Built-in microscale electrostatic fields induced by anatase-rutile-phase transition in selective areas promote osteogenesis, NPG Asia Mater. 8 (2016).
[17] G. Eng, B.W. Lee, L. Protas, M. Gagliardi, K. Brown, R.S. Kass, G. Keller, R.B. Robinson, G. Vunjak-Novakovic, Autonomous beating rate adaptation in human stem cell-derived cardiomyocytes, Nat. Commun. 7 (2016) 10312–10318.
[18] I.E. El-Hakim, A.M.A. Azim, M.F.A. El-Hassan, S.M. Maree, Preliminary investigation into the effects of electrical stimulation on mandibular distraction osteogenesis in goats, Int. J. Oral Maxillofac. Surg. 33 (2004), 0-47.
[19] X. Huang, J. Xing, Z. Wang, J. Han, R. Wang, C. Li, C. Xiao, F. Lu, J. Zhai, Z. Zhou, 0D/1D heterojunction implant with electro-mechanobiological coupling cues promotes osteogenesis, Adv. Funct. Mater. 31 (2021), 2106249.
[20] B. Tang, J. Zhuang, L. Wang, B. Zhang, S. Lin, F. Jia, L. Dong, Q. Wang, K. Cheng, W. Weng, Harnessing cell dynamic responses on magnetoelectric nanocomposite films to promote osteogenic differentiation, ACS APPL MATER INTER 10 (2018) 7841–7851.
[21] M. Lian, B. Sun, Z. Qiao, K. Zhao, X. Zhou, Q. Zhang, D. Zou, C. He, X. Zhang, Bi-layered electrospun nanofibrous membrane with osteogenic and antibacterial properties for guided bone regeneration, Colloids Surf. B Biointerfaces 176 (2019) 219–229.
[22] J. Chen, L. Qiu, Q. Li, J. Ai, H. Liu, Q. Chen, Rapid hemostasis accompanied by antibacterial action of calcium crosslinking tannic acid-coated mesoporous silica/silver Janus nanoparticles, Mater Sci Eng C Mater Biol Appl 123 (2021), 111958.
[23] E. Prajatelistia, N.D. Sanandiya, A. Nurrochman, F. Marseli, S. Choy, D.S. Hwang, Biomimetic Janus chitin nanofiber membrane for potential guided bone regeneration application, Carbohydr. Polym. 251 (2021), 117032.
[24] B. Ma, J. Han, S. Zhang, F. Liu, S. Wang, J. Duan, Y. Sang, H. Jiang, D. Li, S. Ge, J. Yu, H. Liu, Hydroxyapatite nanobelt/polylactic acid Janus membrane with osteoinduction/barrier dual functions for precise bone defect repair, Acta Biomater. 71 (2018) 108–117.
[25] L. Yuan, S. Linlin, J. WT, The investigation of ZnO/Poly(vinylidene fluoride) nanocomposites with improved mechanical, piezoelectric, and antimicrobial properties for orthopedic applications, J Biomed Nanothchnol 14 (2018) 536–545.
[26] X. Dai, B.C. Heng, Y. Bai, F. You, X. Sun, Y. Li, Z. Tang, M. Xu, X. Zhang, X. Deng, Restoration of electrical microenvironment enhances bone regeneration under diabetic conditions by modulating macrophage polarization, Bioact. Mater. 6 (2021) 2029–2038.
[27] B. Tang, B. Zhang, J. Zhuang, Q. Wang, L. Dong, K. Cheng, W. Weng, Surface potential-governed cellular osteogenic differentiation on ferroelectric polyvinylidene fluoride trifluoroethylene films, Acta Biomater. 74 (2018) 291–301.
[28] D. Khare, B. Basu, A.K. Dubey, Electrical stimulation and piezoelectric biomaterials for bone tissue engineering applications, Biomaterials 258 (2020), 120280.
[29] Z. Zhou, W. Li, T. He, L. Qian, G. Tan, C. Ning, Polarization of an electroactive functional film on titanium for inducing osteogenic differentiation, Sci. Rep. 6 (2016), 35512.
[30] X. Zhang, C. Zhang, Y. Lin, P. Hu, Y. Shen, K. Wang, S. Meng, Y. Chai, X. Dai, X. Liu, Nanocomposite membranes enhance bone regeneration through restoring physiological electric microenvironment, ACS Nano 10 (2016) 7279–7286.
[31] M. Guo, A.F. Pegoraro, A. Mao, E.H. Zhou, P.R. Arany, Y. Han, D.T. Burnette, M.H. Jensen, K.E. Kasza, J.R. Moore, F.C. Mackintosh, J.J. Fredberg, D.J. Mooney, J. Lippincott-Schwartz, D.A. Weitz, Cell volume change through water efflux impacts cell stiffness and stem cell fate, Proc. Natl. Acad. Sci. U. S. A. 114 (2017) E8618–E8627.
[32] C. Zhang, W. Liu, C. Cao, F. Zhang, Q. Tang, S. Ma, J. Zhao, L. Hu, Y. Shen, L. Chen, Modulating surface potential by controlling the beta phase content in poly(vinylidene fluoridetrifluoroethylene) membranes enhances bone regeneration, ADV HEALTHC MATER 7 (2018) e1701466–e1701476.
[33] Z. Liu, X. Wan, Z.L. Wang, L. Li, Electroactive biomaterials and systems for cell fate determination and tissue regeneration: design and applications, Adv. Mater. 33 (2021), 2007429.
[34] M.C. Kim, C. Kim, L. Wood, D. Neal, R.D. Kamm, H.H. Asada, Integrating focal adhesion dynamics, cytoskeleton remodeling, and actin motor activity for predicting cell migration on 3D curved surfaces of the extracellular matrix, Integr Biol (Camb) 4 (2012) 1386–1397.
[35] D.D. Schlaepfer, S.K. Mitra, D. Ilic, Control of motile and invasive cell phenotypes by focal adhesion kinase, Biochim. Biophys. Acta 1692 (2004) 77–102.
[36] Z. Chen, T. Klein, R.Z. Murray, R. Crawford, J. Chang, C. Wu, Y. Xiao, Osteoimmunomodulation for the development of advanced bone biomaterials, Mater. Today 19 (2016) 304–321.
[37] Z. Wang, X. He, B. Tang, X. Chen, L. Dong, K. Cheng, W. Weng, Polarization behavior of bone marrow-derived macrophages on charged P(VDF-TrFE) coatings, Biomater. Sci. 9 (2021) 874–881.
[38] V.F. Cardoso, R.G. Correia, J.G. Rocha, S. Lanceros-Mendez, G. Minas, Design and fabrication of piezoelectric microactuators based on β-poly (vinylidene fluoride) films for microfluidic applications, Annu Int Conf IEEE Eng Med Biol Soc (2010) 903–906, 2010.
[39] D.D. Pei, J.L. Sun, C.H. Zhu, F.C. Tian, K. Jiao, M.R. Anderson, C. Yiu, C. Huang, C.X. Jin, B.E. Bergeron, J.H. Chen, F.R. Tay, L.N. Niu, Contribution of mitophagy to cell-mediated mineralization: revisiting a 50-year-old conundrum, Adv. Sci. 5 (2018) 1800873–1800886.
[40] K. Yizhak, S.E. Le Dévédec, V.M. Rogkoti, F. Baenke, V.C. de Boer, C. Frezza, A. Schulze, B. van de Water, E. Ruppin, A computational study of the Warburg effect identifies metabolic targets inhibiting cancer migration, Mol. Syst. Biol. 10 (2014) 744.